NDT&E International 130 (2022) 102649

Contents lists available at ScienceDirect

NDT and E International

journal homepage: www.elsevier.com/locate/ndteint

Lamb wave mode spectroscopy on complex structures with amplitude-based feature detection

Frederick A.F. Purcell *, Matthew R. Pearson, Mark J. Eaton, Rhys Pullin

Cardiff School of Engineering, Cardiff University, Cardiff, CF24 3AA, UK

ARTICLE INFO

Keywords:
Wavenumber
Wave mode spectroscopy
Lamb waves
Mode filtering
Damage detection
NDT
3D structures

ABSTRACT

The need for fast and effective Non-Destructive Testing (NDT) techniques is ever present. Existing techniques such as ultrasonic testing, whilst established and reliable, face many limitations when considering large structures such as those found in the aerospace and green energy sectors. Wave mode, as well as other wavenumber based filtering techniques have been presented to address many of these limitations. This work describes a novel application of Wave Mode Spectroscopy (WMS) along with feature detection for complex geometric shapes. The specimen's geometry is found during the wavefields measurement through the use of a 3D Scanning Laser Doppler Vibrometer (SLDV) allowing the wavefield to be mapped to a 2D plane with limited distortion of the wavelength and without any prior knowledge of the part's geometry. This was shown to allow WMS to be applied to continuous, multi-frequency wavefields and generate accurate thickness maps. Monogenic signal analysis has been applied to the same measurement data to generate amplitude maps that allow the automatic detection of edge features through the use of a Canny edge detection algorithm.

1. Introduction

The ever-increasing use of advanced structures in industries such as aerospace and green energy has placed new demands on excising Non-Destructive Testing (NDT) techniques. NDT is a key tool in informing Structural Health Monitoring (SHM) decisions and allows the life span and safety of structures to be improved, while reducing running costs by providing detailed information about service needs [1]. Higher quality NDT allows for in-service damage to be identified at earlier stages and with higher accuracy whilst also offering the ability to perform quality control post-manufacture, ensuring all parts meet the required standards. The scale as well as limited access to many of these structures, such as wind turbines, can make existing techniques such as contact Ultrasonic Testing (UT) less than ideal. The contact nature of an NDT method such as UT requires costly downtime and full access to the structure. The complex geometry of these structures can further complicate the task of performing a measurement. Driving the probe over a surface is either a very manual process or requires high levels of automation. While non-contact methods have been developed they still require a probe to be held at a set distance from the surface of the material [2].

Recent work has shown wavenumber based full-field techniques as a promising full non-contact NDT method [3–7]. So far, this work has been limited to flat plate-like structures. Extending this technique to complex geometries introduces several complications. The basis of these techniques relies on the ability to accurately determine the wavenumber of a guided Lamb wave and thereby visualise material thickness changes through identifying changes in wavenumber. When measuring the wavefields from a single observation point the observed wavelength will change depending on the angle between the observer and the plane of the specimen. This was demonstrated in work by Koskelo et al. [8].

Work has been completed on pipe structures or structures with very large radii of curvature [4,9,10]. In the cases of large radii of curvature, like those commonly found in structures such as aircraft wings, surfaces were assumed to be flat. This assumption has a negligible effect on the estimation of the wavelength with the A_0 mode wavelengths being on the scale of tens of millimeters for common material thicknesses and frequency ranges. In the work employing wavenumber related techniques on pipe structures Laser Doppler Vibrometers (LDV) or Scanning Laser Doppler Vibrometer (SLDV) systems were being used meaning the pipes were being measured and periodically rotated [10–12] to allow capture of full wavefield data. Geometries such as the cylinder of a pipe fall into the category of developable surfaces. A developable surface can be defined as any surface with a Gaussian curvature of zero, in other

* Corresponding author.
E-mail address: PurcellFA@cardiff.ac.uk (F.A.F. Purcell).

https://doi.org/10.1016/j.ndteint.2022.102649
Received 9 May 2021; Received in revised form 27 March 2022; Accepted 28 March 2022
Available online 18 April 2022

words any surface that can be flattened onto a 2D plane without any distortion [13]. It can be thought of as a surface shape that could be created by bending a piece of paper. Therefore, developable surfaces allow wavefields to be mapped onto a 2D plane without distortion of wavelength. As wavelength is being used to determine thickness this directly relates to the accuracy of this technique. It is also of particular importance in thicker parts where small changes in wavenumber can relate to significant thickness causing small errors in estimation to lead to large errors in thickness estimation.

Work by Spytek et al. [14] aimed to further wavenumber mapping approaches to non-developable complex structures. In their work a SLDV was used. While this allows the laser to be driven over the surface of a structure it cannot differentiate between in-plane and out-of-plane displacement. To complete the measurement of a complex surface they had to realign the specimen to the SLDV multiple times to allow the SLDV to measure the wavefield on different areas. To account for variable geometry a nonuniform Fourier Transform (FT) was applied over each measurement area. As a SLDV system is used this requires prior knowledge of the specimen's geometry as well as known alignment between the specimen and the SLDV, which further complicates setup. While the use of a nonuniform FT allows for certain structures to be measured using wavenumber-based techniques it does not account for distortion present when non-conformal geometries are presented. The use of a 3D SLDV makes this step substantially simpler as a good estimate of the 3D spatial coordinates of each measurement point are known.

While developable surfaces can be mapped onto a 2D plane without distortion this is not an arbitrary task when considering parts that do not have the same level of symmetry or consistent curvature as that found in pipes. Consider for example a surface that has curvature with both positive and negative radii and curvature of variable radii, such as the surface geometry found at the base of a wind turbine blade. Correcting this distortion on a wavefield is a non-arbitrary task.

For in-situ tests a setup is proposed where a 3D SLDV can be placed some distance from the area to be measured. Ultrasonic energy is then driven into the structure using either a contact transducer, air coupled transducer or pulsing laser ultrasound. The use of a 3D SLDV system allows for an estimate of the specimen's shape to be extracted using triangulation alongside the recording of the wavefield.

This paper proposes the use of mapping algorithms to utilise the geometric information obtained by the 3D SLDV to map the wavefield of complex geometries onto a 2D plane so that Wave Mode Spectroscopy (WMS) can be performed. This means no prior knowledge of the specimen or its position relative to the 3D SLDV needs to be known, representing a significant step towards real world application.

While non-developable surfaces only account for a small proportion of the surfaces found on structures such as aircraft or wind turbines they are also considered. By definition distortion will be present when mapping these surfaces onto a 2D plane. An algorithm is chosen to minimise distortion and give the most accurate estimate of wavelength.

In order to isolate the problem of geometrical complexity only isotropic materials were considered in this work. The complexities introduced by differing dispersion of non-isotropic structures are considered in a different piece of work. The nature of the solutions will allow them to be combined into a single solution that is able to examine both isotropic and non-isotropic structures.

Wave mode mapping has been shown to give accurate thickness maps with high spatial and depth resolution, however the clear definition of some edge features can still be challenging. This has been the case for a broad range of wavenumber based techniques [3,6,7,15]. As such the use of monogenic signal analysis is proposed to generate a local amplitude map from which edge features are extracted using Canny edge detection. The detected features can then be shown alongside thickness estimates to help visualise and size structural features and potential damage. A novel and robust complete imaging approach is presented in this work. No prior knowledge about the part's position relative to the SLDV or about its geometry is required. Furthermore, a novel edge detection algorithm is presented to work in conjunction with wave mode mapping to give further clarity to the results. As such this work represents a significant step towards practical real-world application of WMS.

2. Materials and methods

A brief summary of WMS is presented along with the As Rigid As Possible (ARAP) mapping processes.

All data used in this work is gathered from continuous, multi-frequency excitation. For continuous excitation a continuous multi-frequency signal is driven into the specimen until a continuous response is achieved. While the signal being sent to the transducer is not in itself continuous it is able to generate a continuous response in the specimen. The multi-frequency continuous signal sent to the transducer is shown in Fig. 1 in both the frequency and temporal domain. Alongside this a sample response from specimen 1 is also shown.

This signal is then repeated without interruption to generate a continuous response. While mode filtering can be applied to transient and single-frequency data wavefields the advantages of continuous multi-frequency excitation are numerous. Most notably the lack of ring-down time needed between measurements when using continuous excitation vastly reduces the time required to gather data and enables future optimisation for speed. The multiple wavelength scales generated by multi-frequency excitation further improves clarity of results and ensures the method does not need to be tuned for specific transducers or thickness ranges of material, further increasing this technique's robustness. A more detailed presentation of WMS on flat surfaces was previously presented [7]. This paper includes more detailed descriptions of each step. The benefits of using multi-frequency excitation in comparison to single-frequency excitation were also shown in this work.

2.1. Mode filtering

Mode filtering of Lamb wave wavefields is used in this work. Multi-frequency wavefield velocity data is collected and placed into a 3D matrix with two spatial and one temporal axis, $u(x, y, t)$. A spatial window, such as a Tukey, or tapered cosine window, is applied at each temporal sample, t, over the spatial data to reduce transient spike at the edge of the wavefield. Using a 3D Fast Fourier Transform (FFT) this data is then moved into the frequency domain as in Equation (1).

$$U(k_x, k_y, \omega) = FFT(u(x, y, t)) \tag{1}$$

k_x and k_y are the wavenumber components in the x and y spatial axes and t is the temporal component. The wavenumber is simply the inverse of wavelength. In order for correct frequency domain data to be generated the sampling frequency must be consistent in all axes.

Using Rayleigh-Lamb Equation, which describes the behavior of Lamb waves, it is possible to generate a matching 3D mode filter, $F_k(k_x, k_y, \omega, d)$, where d is the thickness value used to solve the Rayleigh-Lamb equations. A filter bank is created using a number of different values for d. Any number of filter widths and filter shapes can be used. It has been shown that selection of these can affect the results [7]. A bandpass width is given by k_{pass} and a flattop filter window shape is used as it has been shown to give good results over a larger range of bandpass widths [7]. Each filter is then multiplied with the measurement data in the frequency domain and then returned to the spatial-temporal domain using an inverse FFT as shown in Equation (2).

$$u(x, y, t; d) = \mathcal{F}_{3d}^{-1}[F_k(k_x, k_y, \omega; d)U(k_x, k_y, \omega)] \tag{2}$$

The Riesz transform, a multi-dimensional extension of the Hilbert transform, can then be used to determine the local amplitude, or envelope, at each time sample after a filter has been applied. The Riesz transform of a real 2D signal, $u(x, y)$, will have three components, as

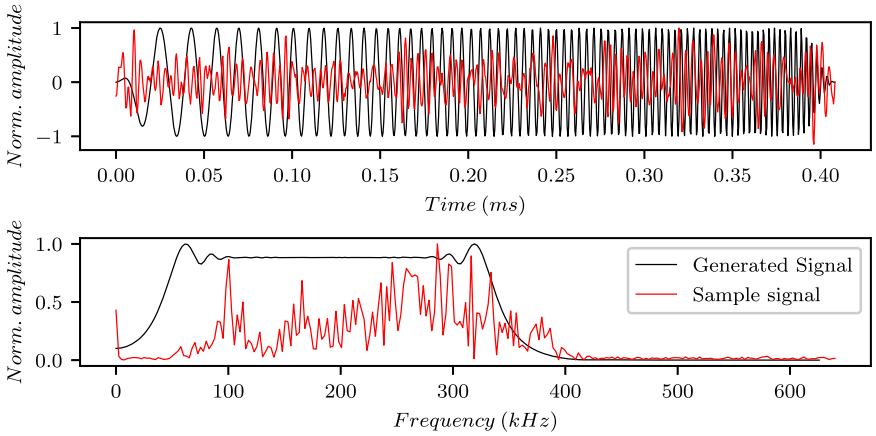

Fig. 1. Transducer signal and sample response from specimen 1 in temporal and frequency domain.

shown in Equations (3)–(5), and is used to find the monogenic signal [16].

$$L_{ox}(k_x,k_y) = j\frac{k_x}{\sqrt{k_x^2+k_y^2}}U(k_x,k_y) \tag{3}$$

$$L_{oy}(k_x,k_y) = j\frac{k_y}{\sqrt{k_x^2+k_y^2}}U(k_x,k_y) \tag{4}$$

$$L(k_x,k_y) = U(k_x,k_y) \tag{5}$$

The amplitude of a 2D matrix is given by equation (6) where $l(x, y)$ is simply the spatial-temporal domain representation of $L(k_x, k_y)$.

$$A(x,y) = \sqrt{l(x,y)^2 + l_{ox}(x,y)^2 + l_{oy}(x,y)^2} \tag{6}$$

Equation (6) can then be applied to find the wavefield amplitude at each time sample of the filtered matrix $u(x, y, t, d)$, giving an amplitude matrix $A(x, y, t, d)$. The resultant matrix is then averaged in the time domain as shown in Equation (7).

$$A(x,y,d) = \sum_t A(x,y,t,d) \tag{7}$$

Each spatial sample (x, y) is then assigned the thickness value d which maximises the amplitude A. This gives a thickness estimate map in the form $d(x, y)$.

The Riesz transform can likewise be applied to the unfiltered wavefield, $u(x, y, t)$, at each time sample, t, before averaging in the time domain to give an amplitude map $A(x, y)$. This will only give a clear image of the amplitude when performed on multi-frequency continuous wavefields. If a transient excitation is used the amplitude map is dominated by the attenuation of the wave as it travels through the structure obscuring other features. Likewise, single-frequency excitation results in a dominant single wavelength resulting in periodic amplitude peaks throughout the structure, again obscuring other features. As such amplitude map images were generated using continuous and multi-frequency excitation which effectively showed boundaries and thickness changes. While the amplitude maps are performed to detect edge features in this work, they will also be sensitive to a number of other factors such as changes in material, dampening due to support structures as well as the distance from the excitation sensor, to name a few. Therefore, further processing of amplitude maps is suggested in this work as well as their use as a complimentary technique to wave mode spectroscopy. When considering large plate structures without edges to reflect the guided waves back, the use of multiple excitation sources would most likely also be required to reduce drop-off in amplitude with increased distance from the transducer.

2.2. Mesh parameterization

This sections presents a method of spatial parameterization that allows an accurate representation of the spatial wavelength to be gained in a structure with a non-conformal geometry.

There are a large number of techniques that map a 3D surface to a 2D plane or vice versa. These have had applications in areas such as computer vision and texture mapping [17]. Different processes have been designed for different purposes and as such offer a number of trade-offs. Authalic mapping aims to preserve the area of each mesh element, whereas conformal mapping aims to preserve the angle and isometric mapping preserves length features [17]. Most mapping algorithms are not solely based on a single principle but a combination of them. This work uses the As Rigid as Possibly (ARAP) process as described by Liu et al. [17]. This algorithm can be found in libigl [18] which is an open source C++ geometry library. The python bindings for libigl were used to implement the ARAP algorithm in this work. The ARAP method was chosen due to its ability to preserve shape, computational speed and simplicity. When considering continuous wavefields, shape distortion is the primary concern that would lead to an inaccurate estimation of spatial wavelength.

Given a mesh of triangles, each triangle has the parameters $x_b = (x_b^0, x_b^1, x_b^2)$, locating it in a plane, where b ranges from $b = 1$ to B which is the total number of triangles present in the mesh [17]. The area of each element of the mesh is given by A_b. Using a piecewise linear function these 3D coordinates of x_t are mapped to a 2D plane and assigned coordinates as $u_b = (u_b^0, u_b^1, u_b^2)$. A number of transformations are used to transform x_b to u_b. $J_b(u)$ denotes a 2x2 Jacobian matrix, which is used to perform this linear transform with auxiliary linear transforms being given by L_b [17]. L_b is one linear transform from a set of allowable transforms M. Equation (8) gives the energy of the paramaterisations [17] where $\|\cdot\|_F$ is the Frobenious norm.

$$E(u,L) = \sum_{n=1}^{b} A_b \|J_b(u) - L_b\|_F^2 \tag{8}$$

This now becomes an optimisation problem where the energy is to be minimised. Minimising the energy ensures as minimises the movement of the points spatially, giving the best 2D representation of the 3D coordinates. Equation (9) shows the optimisation problem faced where $L = L_1, L_2, \ldots, L_B$, L being an allowable linear transform [17].

$$(u,L) = argmin_{(u,L)} E(u,L) \tag{9}$$

Conformal mapping is not desirable in this application as scaling factors can distort triangles, as such losing length data for a triangle which is of key importance when identifying small changes in wavenumber in the wavefield. As such, for ARAP mapping the allowable

transforms, M, are defined by Equation (10) [17]. These are 2D transforms performed on the triangles of the mesh.

$$M = \left\{ \begin{pmatrix} cos\theta & sin\theta \\ -sin\theta & cos\theta \end{pmatrix} : \theta \in [0, 2\pi] \right\} \tag{10}$$

This is an extensive topic, and a more detailed explanation is not within the scope of this paper. More detailed information on the geometric transform used can be found in work by Liu et al. [17].

A further useful concept when considering geometric transforms is Gaussian curvature. Developable surfaces, by definition, have a Gaussian curvature of zero [19]. The curvature is the inverse of the radius which best describes the curvature in an axis at that point [19]. Gaussian curvature, K, is given by the product of the two principal curvatures k_1 and k_2, as shown in Equation (11).

$$K = k_1 k_2 \tag{11}$$

After mapping coordinates onto a 2D plane the distance between the measurement points can vary greatly. Before performing a 3D FFT the spatial samples were re-sampled over an evenly spaced grid using a cubic spline as described by Dierckx [20]. The data could then be placed into a 3D matrix with two spatial and one temporal axis in the form of $u(t, x, y)$. Once in this form it was processed using WMS as previously described [7]. The z axis values of the original coordinates were then interpolated over the evenly spaced grid used to calculate the thickness map. This allowed the results to be shown in the form of a 3D surface plot.

2.3. Experimental setup

A Polytec PSV-500-3D-M 3D SLDV was used to capture the velocity at a number of discreet points on the structure. 100 measurements were captured at each spatial sample point and averaged in the time domain to improve the signal to noise ratio. A temporal sampling frequency of 2.56 MHz was used with a sample length of 1024 samples. Two specimens were used to demonstrate this process. Specimen 1 is a 3 mm thick curved aluminium plate with three 30 mm diameter circular areas where the thickness is reduced to 1 mm, 1.5 mm and 2 mm. The specimen was curved with the defects on the concave face. With an arc height of 40 mm the radius of curvature was approximated to be 210 mm. The measurement area of specimen 1 was 258 mm by 267 mm with a spatial sampling frequency of 954 m^{-1}. The specimen was excited using a 30 kHz–350 kHz Frequency Modulated (FM) signal at 200Vpp, which was driven into the specimen through a single Pancom Pico-z PZT transducer which was super-glued to the specimen. This signal was continually repeated at a rate of 2.45 kHz to generate a continuous excitation. Each repetition of the signal was windowed using a Tukey window to ensure no high frequency transient spikes between repetitions. The Pancom Pico-z transducer has a resonant range of 200 kHz–500 kHz. While the excitation range lies outside of the resonance range of the transducer a signal is still generated, just at a lower amplitude. This can be seen in Fig. 1. While it would be optimal to use a transducer that fully covered the excitation range, the frequency domain nature of the mode filtering method means that, even while certain frequencies will have lower amplitude, their information will still be utilised. The signal was generated with a Red Pitaya STEMLab 125-14 board and a Krohn-Hite 7500 amplifier.

The time to record the response map was about 6 h. This was mainly due to a lack of optimisation of the measurement for speed. If continuous measurement had been employed the same data could have been recorded in about 50 min. With further optimisation it has been shown that single-frequency wavefield data can be captured on the scale of tens of seconds per m^2 [21]. For multi-frequency excitation it is estimated that measurement times would be on the scale of tens of minutes per m^2 are well within reach by reducing the number of averages taken at each point.

A second specimen, specimen 2, is an aluminium panel removed from a Hawk jet. It has a nominal thickness of 0.75 mm with regions of 1.75 mm and 1.5 mm thickness. Likewise, it was excited using a 30 kHz–350 kHz FM signal at 200Vpp, which drove two Vallen System VS900-M PZT transducers with a resonant range of 100 kHz–900 kHz. These transducers were clamped to the structure, with grease used as a coupling agent. Specimen 2 also had a hatch in the measurement area. The thickness of the hatch material was 1.75 mm. It was attached with three screws and a silicate sealant. The scan area was 477 mm by 291 mm with a spatial sampling frequency of 839 m^{-1}. The sampling frequencies of both specimens were high enough to ensure that the Nyquist frequency requirements were met. It is however worth noting that this would not be the case for very thin parts. The problem of the wavenumber falling outside of the expected range is in part dealt with by using a multi-frequency excitation, which ensures a range of wavenumbers. To allow for a greater range of thicknesses a broader frequency range could be used.

As well as the measurement data, geometric data was taken from the 3D SLDV. This data is generated through the 3D alignment of the lasers as well as the 3D triangulation that is performed at every tenth scan point. During 3D alignment each laser head is turned off individually and the vision system of the 3D SLDV confirms the alignment of all three lasers onto the same point. This information further updates the geometric model generated during laser alignment at the time of setup, which is exported in the form of a triangular mesh once the measurement is completed. Images of the rear faces of both specimens 1 and 2 are shown in Fig. 2.

3. Results and discussion

3.1. Specimen 1 results

A frequency domain filter with a bandpass width of $k_{pass} = 100\ m^{-1}$ was applied and filters were calculated at thicknesses, d, between 0.25 mm and 3.25 mm in 0.125 mm intervals. Mode filters were calculated using a flattop shaped window. To show the benefits of ARAP mapping the results were first found using only the x and y coordinates. The coordinates were translated as to minimise the angle between the bottom corners. As before all x and y spatial coordinates were re-sampled using a cubic spline to give evenly spaced data points before a FFT was applied. Fig. 3 (a) shows the wave mode filtered results of specimen 1 using only the x and y coordinates. Fig. 3 (b) on the other hand shows the results where wave mode filtering was performed after the coordinates of the measurement points had been projected onto a 2D plane using the ARAP algorithm.

The first notable issue when not mapping coordinates onto a 2D plane is the decrease in length in the x axis. The length in the x axis is measured to be 247 mm without mapping in comparison to 258 mm when the geometry is flattened using ARAP mapping. Without mapping, the centre of the specimen is estimated to be 2.75 mm thick with a reduction of thickness down to 2.5 mm at the edges. As the angle between the specimen and the vibrometer increases, the wavelength appears to shorten, corresponding to a lower thickness. Depending on the direction of propagation this effect would vary when using transient excitation. Fig. 4 shows a cross section at $y = 135$ mm.

When coordinates are corrected using ARAP mapping the thickness of the plate structure is estimated to be between 2.75 mm and 3 mm. The central area, where the thickness is estimated to be 2.75 mm, was confirmed as having reduced thickness, likely due to the roll bending process. The non-mapped results correctly estimate the area in the center of the specimen around 80 mm $< x <$ 190 mm, where the specimen is perpendicular to the SLDV but then indicates reduced thickness towards the edges where the true thickness actually increases.

Once a flat projection of 3D coordinates had been determined and thickness results found, z axis coordinates were interpolated over the new x and y coordinates. These were then mapped as a surface with the

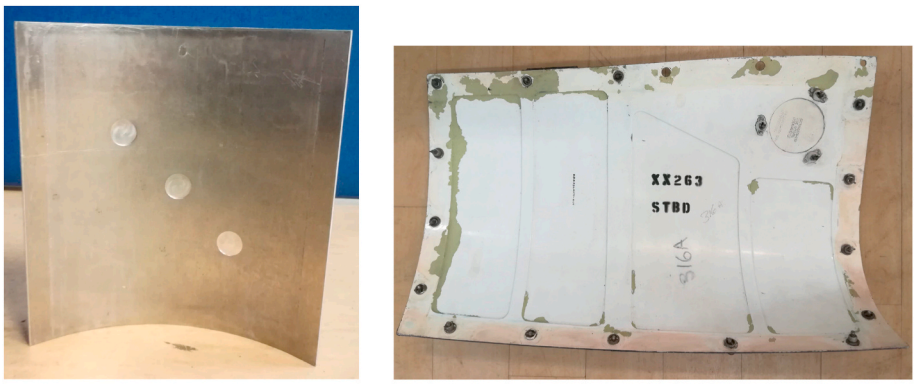

Fig. 2. Rear faces of (a) specimen 1 and (b) specimen 2.

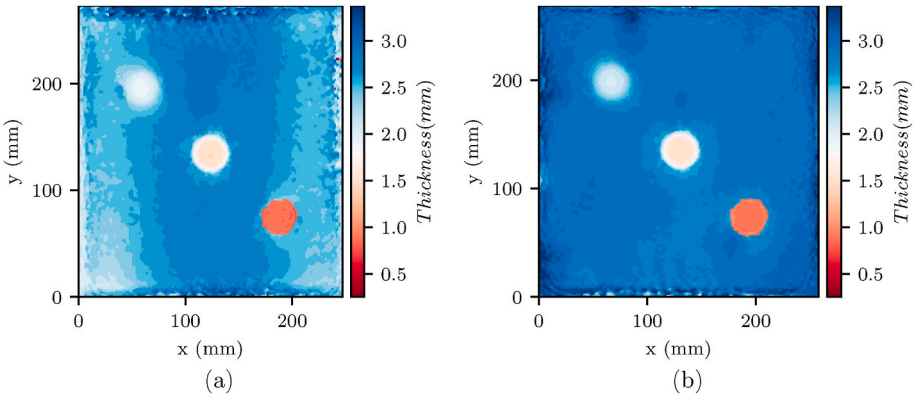

Fig. 3. Specimen 1 results (a) non-mapped (b) ARAP mapped.

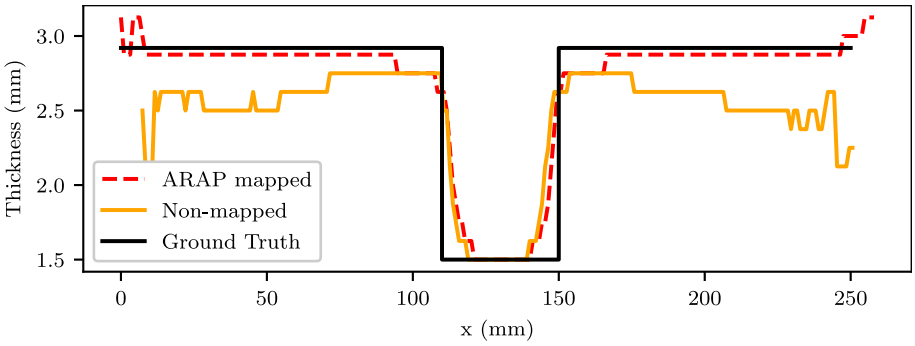

Fig. 4. Specimen 1 cross section at $y = 135$ mm.

thickness results. This is shown in Fig. 5. Some distortion is visible due to errors in the triangulation of 3D coordinates. This is particularly prone to occur at the edges but may also happen anywhere within the measurement area. While this technique is not intended to be used to measure surface geometries a further setup step of using known reference points to calibrate the triangulation could be employed to improve accuracy and reduce distortion.

A local amplitude map was also calculated for this specimen using the ARAP mapped coordinates and is shown in Fig. 6. The envelope of the wavefield was found using Equation (6) at each time sample and then averaged in the time domain.

The three thickness reductions are clearly shown with good definition of the defect edges. The largest thickness reduction shows the highest amplitude with a decrease in amplitude shown at the greatest material thickness. Full continuous excitation is achieved allowing clear identification of geometrical features and no areas of high amplitude are visible around the transducer location. Amplitude maps generated from transient signals give little insight as the amplitude drops significantly whilst the signal travels away from the source and attenuates, preventing any clear identification of features. Continuous excitation ensures energy is distributed fully around the structure. However, if this is done using a single-frequency, peaks and troughs develop on a scale of the wavelength of the wave in the material. These amplitude features then obscure any geometric features. As such, continuous multi-frequency excitation is needed to generate clear amplitude maps. When considering mode filtered results some edges show a gradual change in thickness. This is particularly noticeable for small thickness changes such as those seen between the 2 mm thick area and the 3 mm

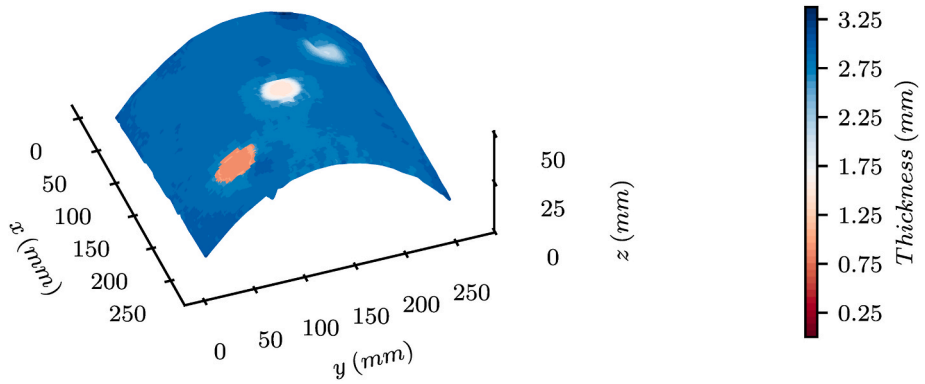

Fig. 5. Specimen 1 ARAP mapped results in 3D.

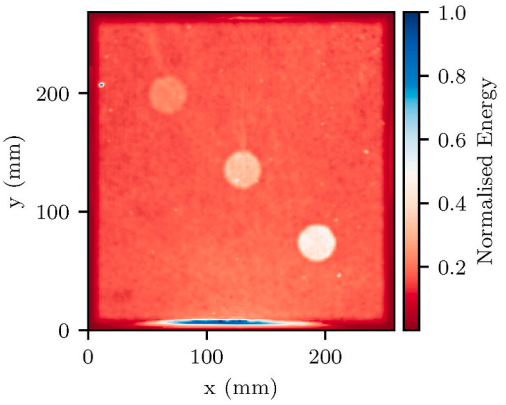

Fig. 6. Specimen 1 local amplitude map.

thick plate in specimen 1. The wavelength of the Lamb wave, along with the spatial sampling frequency means that determining these small and instantaneous thickness changes can be challenging. At a frequency of 125 kHz the A_0 mode has a wavelength of 13.4 mm in 3 mm thick aluminium. Considering this and the fact that spatial samples are separated by over 1 mm it is clear identifying wavelength changes within a single sample is challenging. A further factor is the mode filter width selected to process this data. Had a larger k_{pass} value been used, this transitional region would have been reduced, but so would have depth resolution. Using the local amplitude map a Canny edge detection algorithm was applied as implemented in OpenCV [22]. Fig. 7 (a) shows the detected edges with a standard deviation of $\sigma = 1.4$. The detected edges can then be shown along with the thickness map generated by mode filtering to help allow the easy identification of geometric features as shown in Fig. 7 (b).

The three thickness changes are clearly identifiable along with an edge around the perimeter of the measurement where the spatial Tukey window was applied. A small number of amplitude artefacts are also identified as edge features. The edge detection shows the small amount of error present at the edges of the defects in the thickness estimation map. The thinning to 1 mm is the largest thickness reduction and shows a sharp transition between the 3 mm and 1 mm thickness. Some area outside of the defect is however incorrectly identified as being 1 mm thick instead of 3 mm thick. As the change in material thickness reduces, thickness estimates show less abrupt thickness change. For the region of 2 mm material thickness a gradual transition is visible between the 2 mm and 3 mm thick regions. The edge detection can mitigate some of the trade-off between spatial and depth resolution by demarcating sudden thickness change. While this would show up defects such as delamination defects that often have sudden thickness changes, it would not be expected to effectively show gradual thickness reductions such as those brought about by corrosion defects.

3.2. Specimen 2 results

A more complex geometry was offered by specimen 2. Again, the results were first found using only the *x* and *y* coordinates projected onto a 2D plane. The spatial coordinates were also interpolated to ensure

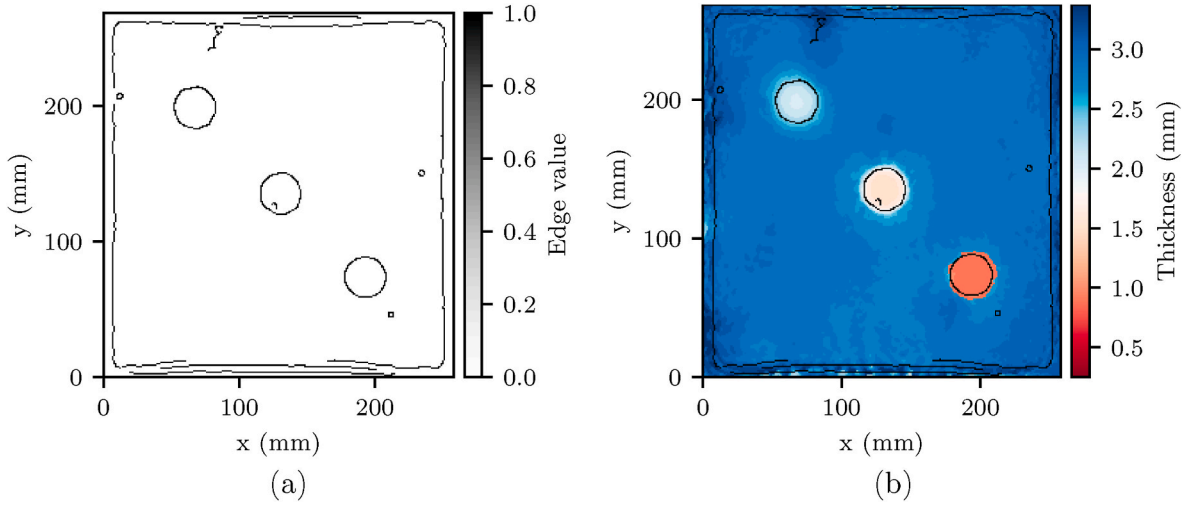

Fig. 7. Specimen 1 (a) Detected edges in the amplitude map and (b) edges overlaid on mode thickness map.

even spatial sampling. Mode filters were calculated using a bandpass width of $k_{pass} = 100\ m^{-1}$ and a flattop shaped window. Filters were centered around thicknesses between 0.25 mm and 2.5 mm at 0.125 mm intervals. Fig. 8 shows the non-mapped and ARAP mapped results.

Using the mapped x and y coordinates z coordinates were re-interpolated over those values. The edges of the results were cropped by ten spatial samples to remove some of the spatial measurement errors present at the edges. Thickness map results are shown with the 3D co-ordinates in Fig. 9.

The un-mapped nature of the results shown in Fig. 8 (a) can be identified from the curved appearance of the stiffeners. The greatest angle between the surface of the specimen and the SLDV are in the region of $y < 100$ mm. This region contains substantial levels of distortion in the non-mapped results shown in Fig. 8 (a). As this area of the specimen is at an angle relative to the SLDV the wavelength would be expected to be interpreted as shorter than its true value. Reduced wavelength, and therefore, increased wavenumber, results in a lower thickness estimate. This is seen across this area with the bulk of the material estimated at a thickness of 0.65 mm and in some places thickness estimates reduce to as low as 0.5 mm. There is also a region of over-estimated thickness between $y < 40$ mm and 150 mm $< x <$ 430 mm. This is likely due to the wavelengths being outside of the range of the wave mode filters.

The fact that the specimen is predominantly curved in a single direction means the wavelength will also mainly appear distorted in one direction. This distortion will be increasingly apparent, the greater the angle between the specimens' surface and the measurement setup.

The nature of the curvature of the specimen can be seen in Fig. 9. Once coordinates were recalculated onto a flat plane using ARAP mapping and mode filtering had been performed, the distortion previously seen in the area of $y < 100$ mm is removed as shown in Fig. 8 (b). The bulk of material is correctly assigned a thickness value of 0.75 mm. The stiffeners are now also shown as being straight. Prior to ARAP mapping being performed the stiffener at $x = 180$ was shown to have reduced thickness at $y < 100$ mm. Post mapping a uniform thickness value of 1.625 mm was assigned to this region.

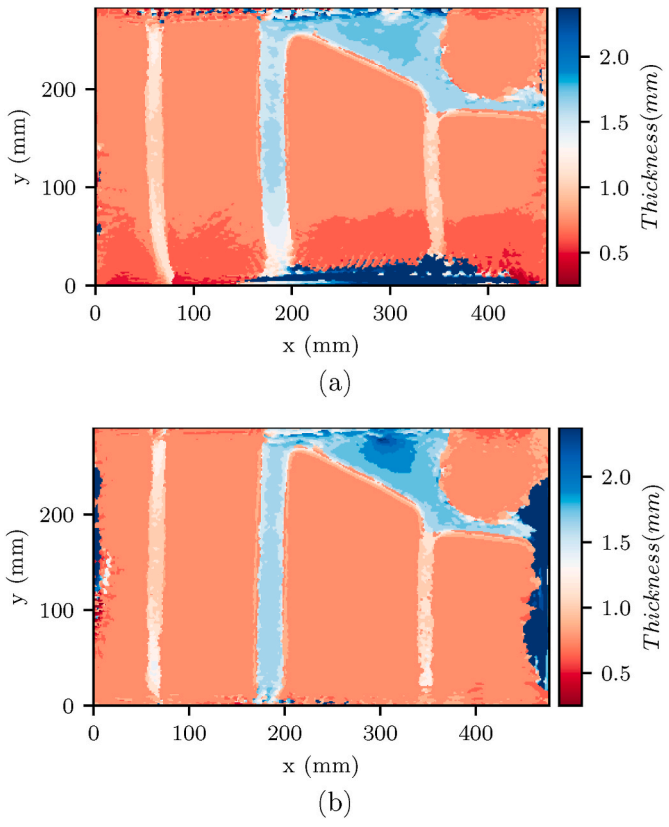

Fig. 8. Specimen 2 results (a) non-mapped (b) ARAP mapped.

Post ARAP mapping being completed, new artefacts are introduced at either end. A small region at $x < 10$ mm is estimated to the largest thickness value, as is a region at $x > 470$ mm. This is largely due to the geometric transformation. As an area over which the wavefield is measured is a rectangle projected onto a complex shape, the measurement area is not rectangular. Without ARAP mapping the x dimension is 460 mm, whereas with mapping it extends to 477 mm. The empty spatial data points that result from mapping the coordinates to a 2D plane are assigned a value of zero in the wavefield. While this accounts for much of the region at either end, which is measured at 2.5 mm, there are still edge artefacts which appear to cause errors a few *mm* further into the measurement area. Spatial windowing is performed after the coordinates are mapped onto a 2D plane; as such there will be a transient shift in the signal causing errors when estimating wavenumber. While applying spatial windowing before ARAP mapping is completed might reduce such artefacts, some artefacts would again be produced by ARAP mapping and the overall shape of the measurement area would change. For measurements of complex geometries, the scan area would need to be cropped post being projected onto a plane to reduce these effects and minimise the amount of lost data at edges.

At $x = 308$ mm and $y = 285$ mm a thickness increase is also shown in the thicker area of the stiffeners. To further explore this, the Gaussian curvature of the surface was calculated for the surface and is shown in Fig. 10.

In the region of $x = 308$ mm and $y = 285$ mm an area of high Gaussian curvature is shown which indicates a measurement artefact, as the surface of the specimen is smooth. Clear triangles are also visible with high curvature at their edges. The number of points used to triangulate the surface geometry by the laser vibrometer is much lower than the number of measurement points. While the use of fewer points allows for a quicker setup time more points would give a much better representation of the surface of the part. The measurement artefacts introduced due to the low sample size did however not seem to have any effect on the thickness estimates in those areas. The edges of the measurement area is particularly susceptible to these types of errors. A low Gaussian curvature across the bulk of the geometry shows that the geometry of the specimen can be mapped to a 2D plane with limited distortion. Several points show higher Gaussian curvature due to measurement errors but seem to introduce limited distortion. The 3D plot given in Fig. 9 also shows the distortion present in the geometrical data causing the distortion at $x = 308$ mm and $y = 285$ mm.

A local amplitude map was determined for specimen 2, using the same process as used for specimen 1, and is shown for in Fig. 11.

The local amplitude map offers a clear view of the geometric features present in the structure. Edges of the thicker stiffener regions are well defined. The hatch and the three bolts holding it to the structure are also visible. Fig. 11 also serves to show the benefits of WMS over pure amplitude-based methods. While stiffeners are clearly visible it is not possible to distinguish a thickness difference between the stiffener at $x = 280$ mm and those at $x = 60$ mm and $x = 350$ mm. The local amplitude map can easily be determined from the data gathered for mode filtering. As such it offers extra information about the geometry or damage in the structure alongside mode filter mapping. Canny edge detection as implemented by OpenCV [22] was again applied to the local amplitude map. Detected edges are shown in Fig. 12 (a). The detected edges were overlaid onto the thickness map determined by the mode filtering process as shown in Fig. 12 (b).

On specimen 2, as well as specimen 1, artefacts are present around the edge of the measurement area. These are due to a combination of the spatial Tukey window applied before filtering as well as the ARAP mapping that results in a non-rectangular measurement area. As local amplitude is not wavelength dependent it is not susceptible to the same distortion seen in wavenumber estimation of complex geometries. As

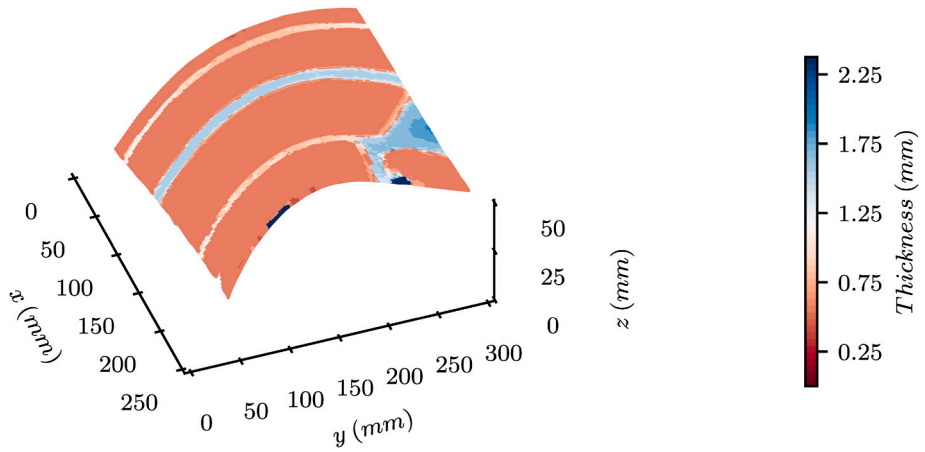

Fig. 9. Specimen 2 ARAP mapped results in 3D.

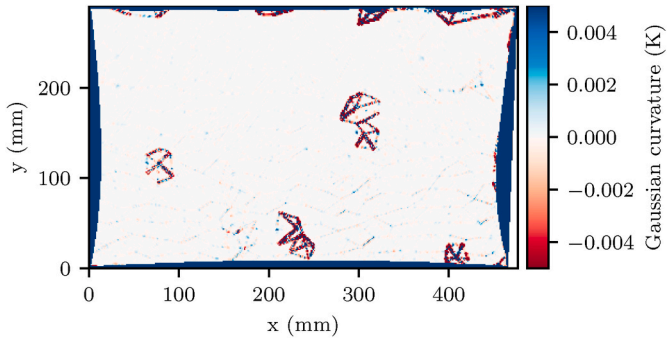

Fig. 10. Specimen 2 Gaussian curvature.

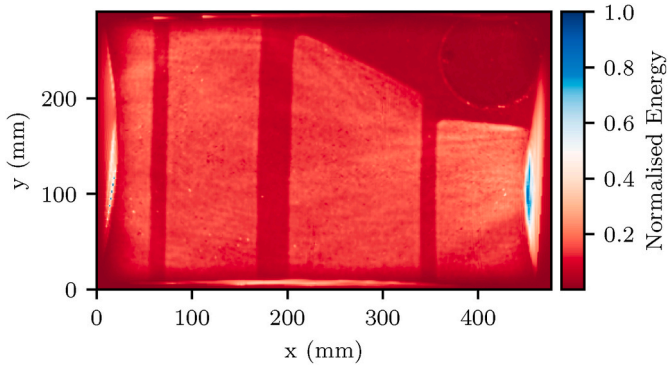

Fig. 11. Specimen 2 local amplitude.

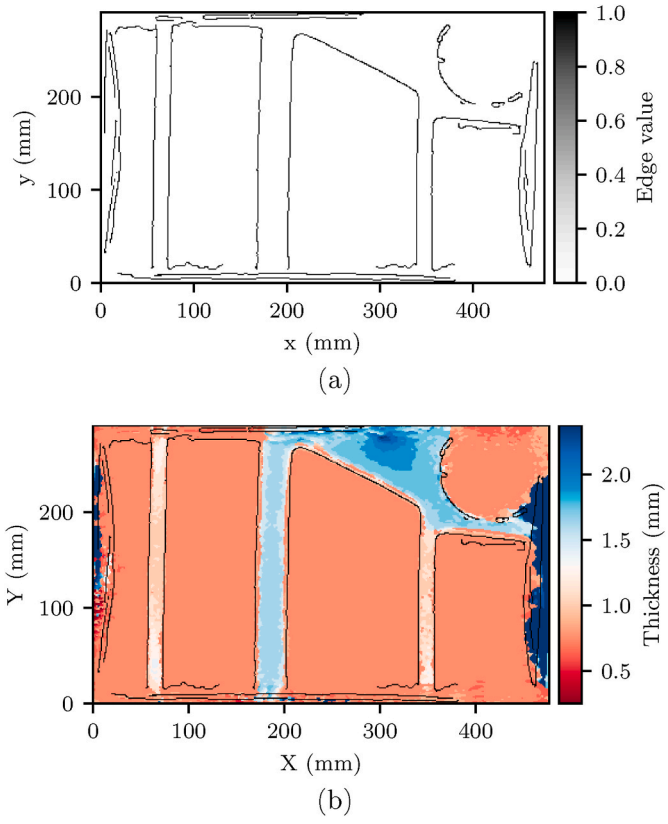

Fig. 12. Specimen 1 (a) Detected edges in amplitude map and (b) edges overlaid on mode thickness map.

such it offers another information source, which helps allow true features and artefacts to be distinguished. Likewise, the local amplitude map is susceptible to amplitude dependant noise, which WMS is not. For instance, an edge is detected around $x = 400$ m and $y = 180$ mm. This does however not relate to any thickness change so can be classed as likely being a measurement artefact. Likewise, the error in thickness estimate seen around $x = 300$ mm and $y = 280$ mm does not coincide with any edges as it is the result of an error in the estimation of the specimens geometry. Edge artefacts are present is all forms of wavenumber filtering and can easily be removed by increasing the measurement area by a small amount and cropping the results. This was not done in this work to show the extent and nature of edge defects. Information on the data underpinning the results presented here, including how to access them, can be found in the Cardiff University data catalogue at http://doi.org/10.17035/d.2022.0177949561.

4. Conclusion

A method was shown where ARAP mapping was employed to map wavefields of complex geometries onto a 2D plane to allow for accurate wave mode mapping to be completed. The parts geometry was extracted from data taken while measuring wavefields using a 3D SLDV, successfully demonstrating a step towards real world application where no prior knowledge of the specimen's geometry or orientation to the 3D SLDV is required. The ability to use the spatial coordinates gathered in the measurement represents a significant advantage compared to other solutions that would require a secondary measurement of the geometry.

The distortion generated in the wavefield by these complex geometries clearly caused errors when performing WMS. This distortion would likewise be present with other methods that rely on the wavelength of Lamb waves for damage detection. Thicker structures would be more greatly affected by any distortion of wavelength due to the reduced change in wavenumber for a given thickness change at larger thicknesses. It was noted that estimation of the geometry had higher errors at the edges of the measurement area. This could however be easily corrected by excluding these regions. A novel use of monogenic signal analysis combined with Canny edge detection was also presented. It was shown that using a continuous multi-frequency excitation allowed for a clear amplitude map to be generated directly from the wavefield data that was free from dominant wavelengths or high amplitude areas due to an attenuating waves traveling through the specimen. This allowed for the Canny edge detection algorithm to be applied to clearly identify sudden changes in thickness. This offers the ability for thickness maps to be compared to known part geometries by referencing edge features.

Author statement

Frederick Purcell: Conceptualization, Data curation, Writing- Original draft preparation, Software, Methodology, Formal analysis.

Matthew Pearson: Conceptualization, Writing- Reviewing and Editing.

Mark Eaton: Conceptualization, Writing- Reviewing and Editing.

Rhys Pullin: Conceptualization, Writing- Reviewing and Editing, Funding acquisition, Supervision.

Declaration of competing interest

The authors declare that they have no known competing financial interests or personal relationships that could have appeared to influence the work reported in this paper.

Acknowledgements

We would like the thank the EPSRC doctoral training program for providing funding for this work. We would also like to thank Paul Leach for machining specimen 1 used in this work and Karin Purcell for helping proof read this work.

References

[1] Mathijsen Django. Innovation in non destructive testing, vol. 60; 2016.
[2] Gholizadeh S. A review of non-destructive testing methods of composite materials. Procedia Struct Integr 2016;1:50–7.
[3] Mesnil O, Leckey Ca, Ruzzene M. Instantaneous and local wavenumber estimations for damage quantification in composites. Struct Health Monit 2014:1–12.
[4] Flynn Eric B, Lee Jr, Jarmer Gj, Park G. Frequency-wavenumber processing of laser-excited guided waves for imaging structural features and defects. In: 6th European workshop on structural health monitoring; 2012. p. 1–8.
[5] Flynn Eric B, Chong See Yenn, Jarmer Gregory J, Lee Jung Ryul. Structural imaging through local wavenumber estimation of guided waves. NDT E Int 2013;59:1–10.
[6] Gao Tianfang, Sun Hu, Hong Yongqiang, Qing Xinlin. Hidden corrosion detection using laser ultrasonic guided waves with multi-frequency local wavenumber estimation. Ultrasonics 2020;108(December 2019):106182.
[7] Purcell Frederick AF, Eaton Mark, Pearson Matthew, Pullin Rhys. Non-destructive evaluation of isotropic plate structures by means of mode filtering in the frequency-wavenumber domain. Mech Syst Signal Process 2020;142:106801.
[8] Koskelo Elise Anne C, Flynn Eric B. Full-field inspection of three-dimensional structures using steady-state acoustic wavenumber spectroscopy. AIP Conf Proc 1806;2017.
[9] Chang Huan-yu. Damage imaging in a stiffened curved composite sandwich panel with wavenumber index via Riesz transform. Structural Health Monitoring; 2019.
[10] Truong Thanh Chung, Lee Jung Ryul. Thickness reconstruction of nuclear power plant pipes with flow-accelerated corrosion damage using laser ultrasonic wavenumber imaging. Struct Health Monit 2018;17(2):255–65.
[11] Kang To, Han Seong Jin, Moon Seongin, Han Soonwoo, Jeon Jun Young, Park Gyuhae. Lamb-wave sparse-frequency interdigital-transducer-based scanning laser Doppler vibrometry for quantitative depth-wise visualization of defects in plates. NDT E Int 2019;107(May):102137.
[12] Rao Jing, Ratassepp Madis, Fan Zheng. Limited-view ultrasonic guided wave tomography using an adaptive regularization method. J Appl Phys 2016;120(19).
[13] Helmut Pottman, Johannes Wallner. Computational line geometry. Berlin: Springer Berlin Heidelberg; 2001.
[14] Spytek Jakub, Mrowka Jakub, Pieczonka Lukasz, Ambrozinski Lukasz. Multi-resolution non-contact damage detection in complex-shaped composite laminates using ultrasound. NDT E Int 2020;116(September):102366.
[15] Flynn Eric B, Stull Nicholas D. Toward utilizing full-field laser-ultrasound for practical nondestructive inspection with acoustic wavenumber spectroscopy. In: 2018 IEEE International Ultrasonics Symposium (IUS), vol. 10. IEEE; 2018. p. 1–7.
[16] Langley Keith, Anderson Stephen J. The Riesz transform and simultaneous representations of phase, energy and orientation in spatial vision. Vis Res 2010;50 (17):1748–65.
[17] Liu Ligang, Zhang Lei, Xu Yin, Gotsman Craig, Gortler Steven J. A local/global approach to mesh parameterization. In: Eurographics Symposium on Geometry Processing. 27; 2008. p. 1495–504. 5.
[18] Jacobsonn Alec, Panozzo Daniele, libigl Other. A simple C++ geometry processing library. 2018.
[19] Stillwell John. Geometry of surfaces. second ed. edition. Stillwell1992: Springer-Verlag New York, Inc.; 1992.
[20] Dierckx P. An algorithm for surface-fitting with spline functions. IMA J Numer Anal 1981;1(3):267–83.
[21] Flynn Eric B, Jarmer GS. High-speed, non-contact, baseline-free imaging of hiddden defects using scanning laser measurements of steady-state ultrasonic vibration. In: 9th International Workshop on Structural Health Monitoring Volume: 1, Number 9th International Workshop on Structural Health Monitoring, vol. 1; 2013.
[22] Bradski G. The OpenCV Library. In: Dr. Dobb's Journal of Software Tools; 2000.